COMPDYN 2011
III ECCOMAS Thematic Conference on
Computational Methods in Structural Dynamics and Earthquake Engineering
M. Papadrakakis, M. Fragiadakis, V. Plevris (eds.)
Corfu, Greece, 25–28 May 2011

DYNAMIC SHAPE RECONSTRUCTION OF THREE-DIMENSIONAL FRAME STRUCTURES USING THE INVERSE FINITE ELEMENT METHOD

Marco Gherlone[1], Priscilla Cerracchio[1], Massimiliano Mattone[1], Marco Di Sciuva[1] and Alexander Tessler[2]

[1] Department of Aeronautics and Space Engineering – Politecnico di Torino,
Corso Duca degli Abruzzi 24, 10129 Torino, Italy
{marco.gherlone, priscilla.cerracchio, massimiliano.mattone, marco.disciuva}@polito.it

[2] Structural Mechanics and Concepts Branch – NASA Langley Research Center,
Mail Stop 190, Hampton, Virginia, 23681-2199, U.S.A.
a.tessler@larc.nasa.gov

Keywords: Shape sensing, Frame structures, Inverse Finite Element Method, Strain gauge.

Abstract. *A robust and efficient computational method for reconstructing the three-dimensional displacement field of truss, beam, and frame structures, using measured surface-strain data, is presented. Known as "shape sensing", this inverse problem has important implications for real-time actuation and control of smart structures, and for monitoring of structural integrity. The present formulation, based on the inverse Finite Element Method (iFEM), uses a least-squares variational principle involving strain measures of Timoshenko theory for stretching, torsion, bending, and transverse shear. Two inverse-frame finite elements are derived using the interdependent interpolations whose interior degrees-of-freedom are condensed out exactly at the element level. In addition, relationships between the order of kinematic-element interpolations and the number of required strain gauges are established. As an example problem, a thin-walled, circular cross-section cantilevered beam subjected to harmonic excitations in the presence of structural damping is modeled using iFEM; where, to simulate strain-gauge values and to provide reference displacements, a high-fidelity MSC/NASTRAN shell finite element model is used. Examples of low and high-frequency dynamic motion are analyzed and the solution accuracy examined with respect to the increased fidelity of the iFEM's discretization and the number of strain gauges.*

1 INTRODUCTION

Real-time reconstruction of structural deformations, using measured strain data, is a key technology for actuation and control of smart structures, as well as for Structural Health Monitoring (SHM) [1]. Known as "shape sensing", this inverse problem is commonly formulated with the assumption that multiple strain sensors at various structural locations provide real-time strain measurements. Most inverse algorithms use some type of Tikhonov's regularization, which is manifested by constraint (regularity) terms that ensure a certain degree of solution smoothness (refer to [2-5] and references therein.)

Most of the shape sensing efforts focused exclusively on beam-bending problems. Davis et al. [6] used optimized trial functions and weights to reconstruct a simple static-beam response from discrete strain measurements. To model more complex deformations, their approach requires a large number of trial functions and strain sensors. Kang et al. [7] used vibration mode shapes to reconstruct the beam response due to dynamic excitation. In their approach, modal coordinates are computed using strain-displacement relationship and measured surface strain measurements; the method requires the same number of mode shapes and strain sensors. Kim et al. [8] and Ko et al. [9] used classical beam equations to integrate the discretely measured strains to determine the deflection of a beam. By regression of experimental strain data and by accounting for the applied loading, Kim et al. [8] obtained a continuous curvature function, leading to the evaluation of the beam deflection. Ko et al. [9] developed a load-independent method by approximating the beam curvature using piece-wise polynomials; the authors demonstrated the validity of this one-dimensional scheme by evaluating the deflection and cross-section twist of an aircraft wing.

To enable shape-sensing analyses of plates undergoing bending deformations, Bogert et al. [10] examined a modal transformation method that allows the development of suitable strain-displacement transformations. The approach makes use of a large number of natural vibration modes. When applied to high-fidelity finite element models, however, the method requires a computationally intensive eigenvalue analysis and a detailed description of the elastic and inertial material properties. Jones et al. [11] employed a least-squares formulation for shape sensing of a cantilever plate, where the axial strain was fitted with a cubic polynomial. The strain field was then integrated with the use of approximate boundary conditions at the clamped end to obtain plate deflections according to classical bending assumptions. Shkarayev et al. [12,13] used a two-step solution procedure: the first step involves the structural analysis of a plate/shell finite element model, and the second, a least-squares algorithm. The methodology reconstructs the applied loading first, which then leads to the displacements. In a series of four papers, Mainçon and co-authors [14-17] developed a finite element formulation that seeks the solution for the displacements and loads simultaneously, requiring a priori knowledge of a subset of applied loading and the material properties. The solution procedure minimizes a cost function consisting of unknown loads and differences between the measured and estimated quantities (displacements or strains); the cost function is regularized by way of equilibrium constraints. The number of unknowns is three times the number of the degrees-of-freedom in the finite element discretization. Importantly, the accuracy of the solution strongly depends on the choice of suitable weights; these are computed from a complex procedure involving the probability distributions of the unknown loads and measured data. In [16,17], sensitivity analyses were carried out for truss structures, investigating variations in the input data as well as the modeling errors. Nishio et al. [18] employed a weighted-least-squares formulation to reconstruct, on the basis of measured strain data, the deflection of a composite cantilever plate. The weighting coefficients in the least-square terms were adjusted in order to account for the inherent errors in the measured strain data. The

weights were computed for the given data-acquisition apparatus, load case, and test article, with the consequent difficulties in generalizing the procedure.

Many of the aforementioned inverse methods either lack generality with respect to structural topology and boundary conditions, or require sufficiently accurate loading and/or elastic-inertial material information – the kind of data that are either unavailable or difficult to obtain outside the laboratory environment; for these reasons, such approaches are generally unsuited for use in on-board SHM algorithms. An algorithm that is well-suited for SHM should be: (1) able to model general structural topologies and boundary conditions (e.g., built-up aircraft structures), (2) robust, stable, and accurate under a wide range of loadings, material systems, inertial/damping characteristics, and inherent errors in the strain measurements, and (3) sufficiently fast for real-time applications.

An algorithm that appears to fulfill the aforementioned requirements, labeled the inverse Finite Element Method (iFEM), was recently developed by Tessler and Spangler [1,19]. The methodology employs a weighted-least-square variational principle which is discretized by C^0-continuous finite elements that accommodate arbitrarily positioned and oriented strain-sensor data. The iFEM framework, providing accurate and stable solutions of the displacement and strain fields for the discretized structural domain, is amenable to any type of structural modeling including frame (truss and beam), plate, shell, and solid idealizations. Because only strain-displacement relations are used in the formulation, both static and dynamic regimes can be modeled without any a priori knowledge of the material, inertial, loading, or damping structural properties. To model arbitrary plate and shell structures, Tessler [20] developed, using the first-order shear-deformation theory, a three-node *inverse shell element* formulation. The numerically generated [20] and experimentally measured-strain data [21,22] were used to assess the formulation's robustness and accuracy.

This paper consolidates the authors' recent efforts in [23-25], presenting the development and assessment of simple and efficient inverse-frame finite elements. The methodology permits effective and computationally efficient shape-sensing analyses to be performed on truss, beam, and frame structures instrumented with strain gauges. The kinematic assumptions are those of Timoshenko shear-deformation theory [26]; they incorporate stretching, torsion, bending, and transverse shear deformation modes in three dimensions. The formulation uses a least-squares variational principle that is specialized from [19] for three-dimensional frame analysis. The variational framework, in conjunction with suitable finite element discretizations involving inverse finite elements, yields a system of linear algebraic equations; the equations are efficiently solved for the unknown displacement degrees-of-freedom (dof's), thus providing the deformed structural-shape predictions.

In the remainder of the paper, the kinematic assumptions for a three-dimensional frame are discussed, followed by the description of the least-squares variational principle suitable for three-dimensional deformations of frame structures. This is followed by a discussion of two C^0-continuous, inverse-frame elements that use the well-established interdependent interpolations that resolve the shear locking effect. Finally, to examine the predictive capabilities of the inverse elements for a given set of distributed strain gauges, shape-sensing studies are carried for a cantilevered beam undergoing harmonic excitations in the presence of structural damping.

2 GOVERNING EQUATIONS

Consider a straight frame member of constant cross-section positioned in the three-dimensional Cartesian coordinates (x,y,z) as depicted in Figure 1; the coordinate origin, O, is located at the cross-section's center of mass, which is also coincident with the shear center. The longitudinal, elastic x-axis is normal to the cross-sectional plane (y, z), where y and z are the

cross-section's principal inertial axes. The frame member has length L and its cross section has area A, area moments of inertia with respect to the y- and z-axis I_y and I_z, respectively, and polar moment of inertia $I_P = I_y + I_z$ (Figure 1). The frame member is made of an isotropic material, represented by the elastic constants: E (Young's modulus), G (shear modulus), and ν (Poisson ratio).

Neglecting the effect of axial warping due to torsion, and assuming the kinematics of Timoshenko theory [26] in three dimensions, i.e., each cross-section remains flat and rigid with respect to thickness-stretch deformations along the y and z axes, gives rise to the three Cartesian components of the displacement vector of the form

$$\begin{aligned} u_x(x,y,z) &= u(x) + z\theta_y(x) - y\theta_z(x) \\ u_y(x,y,z) &= v(x) - z\theta_x(x) \\ u_z(x,y,z) &= w(x) + y\theta_x(x) \end{aligned} \tag{1}$$

where u_x, u_y, and u_z are the displacements along the x, y, and z axes, respectively, with u, v, and w denoting the displacements at $y = z = 0$; θ_x, θ_y, and θ_z are the rotations about the three coordinate axes. The positive orientations for the six *kinematic variables*, $\mathbf{u} \equiv \left[u, \quad v, \quad w, \quad \theta_x, \quad \theta_y, \quad \theta_z\right]^T$, are depicted in Figure 1.

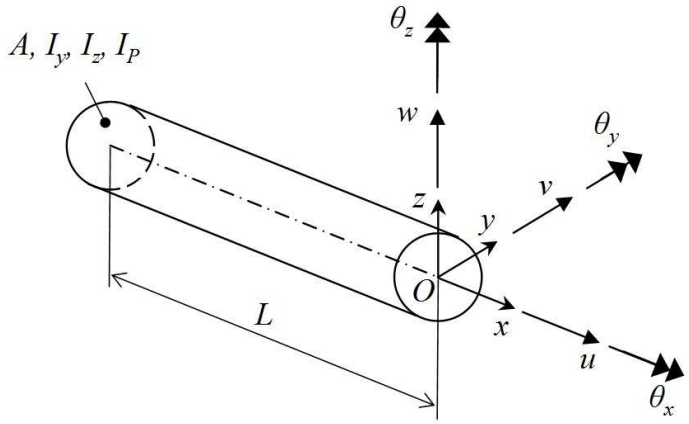

Figure 1: Beam geometry and kinematic variables.

Adhering to the small-strain hypothesis, the non-vanishing strain components have the form

$$\begin{aligned} \varepsilon_x(x,y,z) &= e_1(x) + z\,e_2(x) + y\,e_3(x) \\ \gamma_{xz}(x,y) &= e_4(x) + y\,e_6(x) \\ \gamma_{xy}(x,z) &= e_5(x) - z\,e_6(x) \end{aligned} \tag{2}$$

where $\mathbf{e}(\mathbf{u}) \equiv \left[e_1, \quad e_2, \quad e_3, \quad e_4, \quad e_5, \quad e_6\right]^T$ denote the strain measures of the theory, related to the kinematic variables by first-order partial differentiation

$$
\begin{aligned}
e_1(x) &\equiv u_{,x}(x) & e_4(x) &\equiv w_{,x}(x) + \theta_y(x) \\
e_2(x) &\equiv \theta_{y,x}(x) & e_5(x) &\equiv v_{,x}(x) - \theta_z(x) \\
e_3(x) &\equiv -\theta_{z,x}(x) & e_6(x) &\equiv \theta_{x,x}(x)
\end{aligned}
\tag{3}
$$

The forces {N, Q_y, and Q_z} and moments {M_x, M_y, and M_z} are related to the strain measures, e_i, by way of the constitutive equations (refer to Figure 2)

$$
\begin{aligned}
\mathrm{N} &= A_x e_1 & \mathrm{M}_x &= J_x e_6 \\
\mathrm{Q}_y &= G_y e_5 & \mathrm{M}_y &= D_y e_2 \\
\mathrm{Q}_z &= G_z e_4 & \mathrm{M}_z &= D_z e_3
\end{aligned}
\tag{4}
$$

where $A_x \equiv EA$ is the axial stiffness, $G_y \equiv k_y^2 GA$ and $G_z \equiv k_z^2 GA$ are the shear stiffnesses (with k_y^2 and k_z^2 shear correction factors), $J_x \equiv GI_P$ is the torsional stiffness, and $D_y \equiv EI_y$ and $D_z \equiv EI_z$ are the bending stiffnesses.

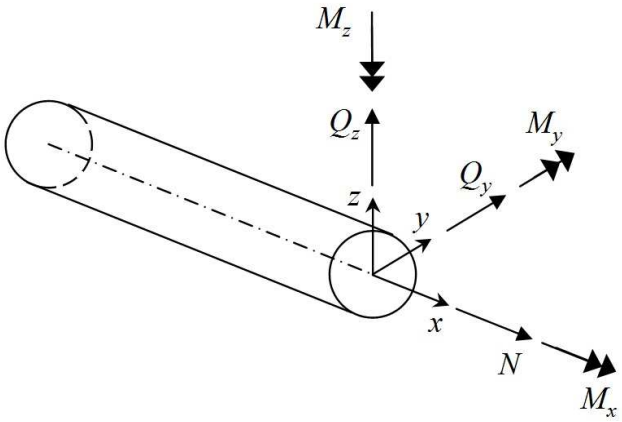

Figure 2: Beam resultant forces and moments.

If $q_x(x)$, $q_y(x)$, and $q_z(x)$ are the distributed loads applied along the *x*, *y* and *z* directions, respectively, the frame-member equilibrium equations become

$$
\begin{aligned}
\frac{\mathrm{dN}}{\mathrm{d}x} &= -q_x & \frac{\mathrm{dM}_x}{\mathrm{d}x} &= 0 \\
\frac{\mathrm{dQ}_y}{\mathrm{d}x} &= -q_y & \frac{\mathrm{dM}_y}{\mathrm{d}x} &= \mathrm{Q}_z \\
\frac{\mathrm{dQ}_z}{\mathrm{d}x} &= -q_z & \frac{\mathrm{dM}_z}{\mathrm{d}x} &= \mathrm{Q}_y
\end{aligned}
\tag{5}
$$

To reconstruct the deformed shape of a frame structure for which certain in-situ strain measurements are known, a functional $\Phi(\mathbf{u})$ that matches, in a least-square sense, the complete set of

the analytic strain measures, $\mathbf{e}(\mathbf{u})$, to those corresponding to the strain measurements, $\mathbf{e}^{\varepsilon}$, is minimized with respect to the kinematic variables, $\mathbf{u}$; where the superscript ε denotes those quantities that are computed from the in situ strain measurements. Thus, the $\Phi(\mathbf{u})$ functional can be written in compact notation as

$$\Phi(\mathbf{u}) = \left\| \mathbf{e}(\mathbf{u}) - \mathbf{e}^{\varepsilon} \right\|^2 \tag{6}$$

$\Phi(\mathbf{u})$ is then discretized by the piecewise-continuous displacements, $\mathbf{u}^h$, i.e.,

$$\mathbf{u}(x) \simeq \mathbf{u}^h = \mathbf{N}(x)\mathbf{u}^e \tag{7}$$

where $\mathbf{N}(x)$ denotes C^0-continuous shape functions and $\mathbf{u}^e$ the nodal dof's. Consequently, the total least-squares functional is a sum of the individual element contributions, $\Phi^e(\mathbf{u}^h)$, i.e., $\Phi = \sum_{e=1}^{N} \Phi^e$, with N denoting the total number of elements. Accounting for the axial stretching, bending, twisting, and transverse shearing, the element functional is given by

$$\Phi^e(\mathbf{u}^h) \equiv \sum_{k=1}^{6} \lambda_k \, \Phi_k^e \tag{8}$$

where

$$\boldsymbol{\lambda} \equiv \left[\lambda_1^0 \quad \lambda_2^0 A^e \quad \lambda_3^0 A^e \quad \lambda_4^0 \quad \lambda_5^0 \quad \lambda_6^0 A^e \right] \tag{9}$$

with $\lambda_k^0 \quad (k = 1,...,6)$ denoting the dimensionless weight coefficients, and A^e the cross-sectional area of the element. The six components of the element functional are given as the Euclidean norms

$$\Phi_k^e \equiv \frac{L^e}{n} \sum_{i=1}^{n} \left[e_k(x_i) - e_k^{\varepsilon i} \right]^2 \quad (k = 1,...,6) \tag{10}$$

where L^e denotes the element length, n is the number of strain sensors, x_i ($0 \le x_i \le L^e$) are the positions at which the strain sensors are located, and the superscript εi is used to denote the strain measures that are computed from the strain-sensor values (experimental values) at the location x_i.

Substituting Eq. (7) into Eq. (3) gives the strain measures in terms of the nodal dof's as

$$\mathbf{e}(\mathbf{u}) = \mathbf{B}(x)\mathbf{u}^e \tag{11}$$

where the matrix $\mathbf{B}(x)$ contains the derivatives of the shape functions $\mathbf{N}(x)$. Substituting Eq. (11) into Eq. (8) results in the following quadratic form

$$\Phi^e = \frac{1}{2}\left(\mathbf{u}^e\right)^T \mathbf{k}^e \mathbf{u}^e - \left(\mathbf{u}^e\right)^T \mathbf{f}^e + \mathbf{c}^e \tag{12}$$

where $\mathbf{k}^e$ and $\mathbf{f}^e$ are defined in terms of $\mathbf{B}(x)$ and $\mathbf{c}^e$ is a constant. Note that $\mathbf{k}^e$ depends only on the measurement locations, x_i, whereas $\mathbf{f}^e$ depends on the experimentally measured strain values. Minimization of the functional Φ^e with respect to $\mathbf{u}^e$ leads to the inverse element matrix equation

$$\mathbf{k}^e \mathbf{u}^e = \mathbf{f}^e \tag{13}$$

The assembly of the finite element contributions, while accounting for the appropriate coordinate transformations and by specifying problem-dependent displacement boundary conditions, results in a non singular system of algebraic equations of the form

$$\mathbf{K}\mathbf{U} = \mathbf{F} \tag{14}$$

The solution of these equations for the unknown dof's is efficient: the **K** matrix is inverted only once, since it is independent of the values of the measured strains. The **F** vector, however**,** is dependent on the measured strain values that change during deformation. Thus, at any strain-measurement update during deformation, the matrix-vector multiplication provides the solution for the unknown nodal displacement dof's, $\mathbf{U} = \mathbf{K}^{-1}\,\mathbf{F}$, where $\mathbf{K}^{-1}$ remains unchanged for a given distribution of strain sensors[1].

The remaining part of the element formulation involves the selection of suitable shape functions, symbolically defined by Eq. (7), and the computation of the experimental strain measures, $e_k^{\varepsilon i}$, appearing in Eq. (10). In Section 3, the shape functions for two alternative inverse-frame elements, each having two nodes and twelve dof's, are derived. In Section 4, a procedure for computing $e_k^{\varepsilon i}$ is described; it relates the number of strain gauges to the interpolation order of the shape functions.

[1] Depending on the selected shape functions (refer to Section 3), interior dof's may be present. These are condensed out at the element level by straightforward partitioning of the element equations, $\mathbf{k}^e\mathbf{u}^e = \mathbf{f}^e$, and then by solving exactly for the condensed dof's in terms of the end-node dof's. This process results in the reduced element equations (without the interior dof's), $\mathbf{k}_R^e\mathbf{u}_R^e = \mathbf{f}_R^e$, where $\mathbf{k}_R^e$ is a function of the partitioned parts of the original $\mathbf{k}^e$ matrix, and $\mathbf{u}_R^e$ contains the end-node dof's. Since the unreduced $\mathbf{k}^e$ matrix is independent of the strain values, so is the $\mathbf{k}_R^e$ matrix. This implies that even for the elements with the condensed-out interior dof's, the corresponding system matrix, $\mathbf{K}$, is also strain-value independent.

3 ELEMENT SHAPE FUNCTIONS

In this section, inverse frame elements of 0^{th} and 1^{st} order are formulated. The elements use the interdependent interpolations that enable excellent predictions even for very slender frame members, without incurring any form of excessive stiffening due to shear locking [27]. The 0^{th}-order shape functions are guided by Timoshenko equilibrium equations, Eq. (5), that correspond to the forces and moments applied exclusively at the end nodes, resulting in constant distributions of the transverse-shear strain measures. The 1^{st}-order shape functions accommodate Eq. (5) for uniformly distributed transverse loads, giving rise to linear distributions of the transverse-shear strain measures.

A frame element is referred to a local axial coordinate $x \in \left[0, L^e\right]$, where L^e denotes the element length. Furthermore, a non-dimensional coordinate $\xi \equiv (2x / L^e - 1) \in \left[-1,1\right]$ is used to define the element shape functions (Figure 3). The initial nodal configurations are defined by the two end nodes, 1 (at $\xi = -1$) and 2 (at $\xi = +1$) and one or three interior nodes. Thus, the initial configuration for the 0^{th}-order element has the interior node, *r* (at the midspan, $\xi = 0$); whereas the interior nodes of the 1^{st}-order element are *q* (at $\xi = -1/2$), *r* (at $\xi = 0$), and *s* (at $\xi = +1/2$).

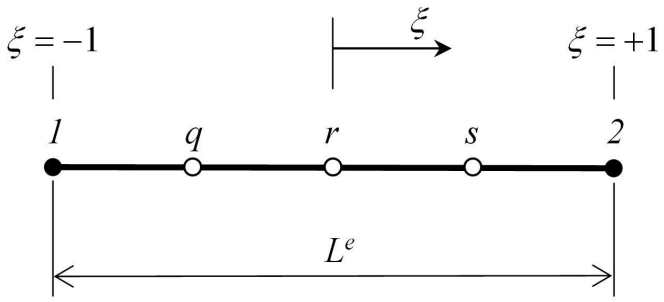

Figure 3: Inverse finite element geometry and nodal topology.

The initial nodal configurations of the 0^{th}- and 1^{st}-order elements are readily reduced to two nodes and twelve dof by condensing out the interior dof's at the element level, Eq. (13), in a manner analogous to static condensation. The resulting elements have three-displacement and three-rotation dof's at each end node (Figure 4)

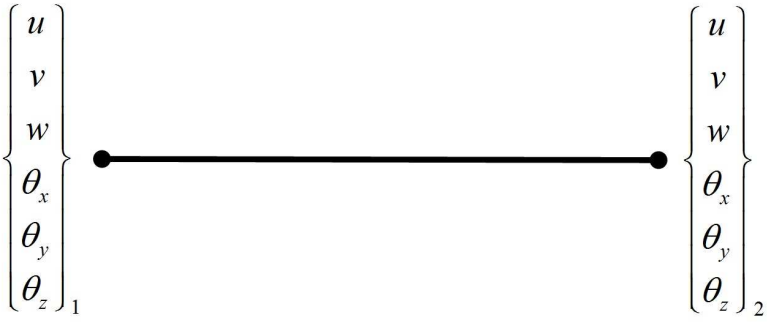

Figure 4: Two-node inverse finite element.

3.1 0^{th}-order element

The formulation of the 0^{th}-order element is guided by Eq. (5) for the loading case of end-node forces and moments. For this case, the axial force, twisting moment, and shear forces are constant along the element; whereas the bending moments are linear. Equations (5) in terms of

the strain measures (after Eq. (4) have been introduced) indicate that the strain measures e_i (i=1, 4-6) are constant, and e_i (i=2,3) are linear. From Eq. (3), it is deduced that u and θ_x are linear, θ_y and θ_z parabolic, v and w cubic.

Thus, u and θ_x are interpolated using the linear Lagrange polynomials $L_i^{(1)}(\xi)\ \ (i=1,2)$

$$\begin{aligned} u(\xi) &= \sum_{i=1,2} L_i^{(1)}(\xi) u_i \\ \theta_x(\xi) &= \sum_{i=1,2} L_i^{(1)}(\xi) \theta_{xi} \end{aligned} \tag{15}$$

The polynomial degrees for the deflection, v and w, and bending rotation, θ_y and θ_z, variables are interrelated: if v and w are defined by cubic polynomials, then θ_y and θ_z need to be represented by quadratic polynomials to form consistent, free of locking, transverse shear-strain measures e_4, e_5 (This is a key requirement of the interdependent interpolation strategy, IIS.) Thus, the remaining kinematic variables, which enable both bending and shear deformation along the x and y orthogonal directions, are interpolated as

$$\begin{aligned} v(\xi) &= \sum_{i=1,2} L_i^{(1)}(\xi) v_i - \sum_{j=1,r,2} N_j^{(3)}(\xi) \theta_{zj} \\ w(\xi) &= \sum_{i=1,2} L_i^{(1)}(\xi) w_i + \sum_{j=1,r,2} N_j^{(3)}(\xi) \theta_{yj} \\ \theta_y(\xi) &= \sum_{j=1,r,2} L_j^{(2)}(\xi) \theta_{yj} \\ \theta_z(\xi) &= \sum_{j=1,r,2} L_j^{(2)}(\xi) \theta_{zj} \end{aligned} \tag{16}$$

where $L_j^{(2)}(\xi)$ are standard quadratic Lagrange polynomials, and $N_j^{(3)}(\xi)\ \ (j=1,r,2)$ are special-form cubic polynomials; these functions are obtained from standard cubic Lagrange polynomials by enforcing the transverse shear-strain measures to be constant along the element, i.e.,

$$\begin{aligned} e_4 &= \left(w_{,x} + \theta_y\right) = const. \\ e_5 &= \left(v_{,x} - \theta_z\right) = const. \end{aligned} \tag{17}$$

The expression for $L_i^{(1)}(\xi)$, $L_j^{(2)}(\xi)$, and $N_j^{(3)}(\xi)\ \ (i=1,2;\ \ j=1,r,2)$ are summarized in the Appendix. The element has fourteen dof's, six at each element end, plus the rotations θ_{yr} and θ_{zr} at the element's midspan

$$\mathbf{u}^e \equiv \left\{u_1,\ v_1,\ w_1,\ \theta_{x1},\ \theta_{y1},\ \theta_{z1},\ \theta_{yr},\ \theta_{zr},\ u_2,\ v_2,\ w_2,\ \theta_{x2},\ \theta_{y2},\ \theta_{z2}\right\}^T \tag{18}$$

Thus, in order to achieve a two-node element with twelve dof's (Figure 4), the internal dof's, θ_{yr}, θ_{zr}, are condensed out statically.

3.2 1st-order element

Consider a frame element loaded by uniformly distributed transverse loads, $q_y(x)$ and $q_z(x)$. From Eqs. (5), after the substitution of Eqs. (4), it is readily deduced that (e_4, e_5) need to be linear and (e_2, e_3) parabolic. The u and θ_x variables remain linear and interpolated by Eq. (15). Moreover, (v, w) and (θ_y, θ_z) are respectively quartic and cubic, and are interpolated as

$$\begin{aligned}
v(\xi) &= \sum_{k=1,q,r,s,2} L_k^{(4)}(\xi)\, v_k \\
w(\xi) &= \sum_{k=1,q,r,s,2} L_k^{(4)}(\xi)\, w_k \\
\theta_y(\xi) &= \sum_{i=1,2} L_i^{(1)}(\xi)\, \theta_{yi} + \sum_{k=1,q,r,s,2} \overline{N}_k^{(3)}(\xi)\, w_k \\
\theta_z(\xi) &= \sum_{i=1,2} L_i^{(1)}(\xi)\, \theta_{zi} - \sum_{k=1,q,r,s,2} \overline{N}_k^{(3)}(\xi)\, v_k
\end{aligned} \tag{19}$$

where $\overline{N}_k^{(3)}(\xi)$ $(k = 1, q, r, s, 2)$ are cubic polynomials that satisfy the conditions (for the detailed expressions, refer to the Appendix)

$$\begin{aligned}
e_4 &= \left(w_{,x} + \theta_y\right) = linear \\
e_5 &= \left(v_{,x} - \theta_z\right) = linear
\end{aligned} \tag{20}$$

Interpolation described by Eqs. (15) and (19) leads to a formulation with eighteen dof's

$$\mathbf{u}^e \equiv \left\{u_1,\ v_1,\ w_1,\ \theta_{x1},\ \theta_{y1},\ \theta_{z1},\ v_q,\ w_q,\ v_r,\ w_r,\ v_s,\ w_s,\ u_2,\ v_2,\ w_2,\ \theta_{x2},\ \theta_{y2},\ \theta_{z2}\right\}^T \tag{21}$$

The interior dof's are condensed out at the element level, leading again to a twelve dof's inverse element (Figure 4).

4 INPUT DATA FROM SURFACE STRAIN MEASUREMENTS

A key step in the iFEM formulation is to compute the strain measures due to experimentally measured surface strains. Herein, the relationships between the measured surface strains and the six strain measures, e_i, are established. Also discussed are strain-gauge positions along the frame axis and their angular orientations that enable the complete description of the experimental strain

measures. The present analysis is restricted to frame members with circular cross sections; the cylindrical coordinate system (θ, x, r) is shown in Figure 5.

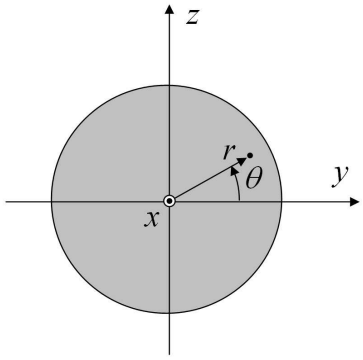

Figure 5: Orthogonal and cylindrical coordinate systems.

4.1 Strain measures from linear strain gauge measurements

Taking the usual assumption of negligible σ_y and σ_z, σ_x and $\tau_{x\theta}$ are the only non-zero stress components acting on the external surface $r = R_{ext}$ (Figure 6(a)). The corresponding strain state is (Figure 6(b))

$$\varepsilon_x = \frac{\sigma_x}{E}, \quad \varepsilon_\theta = -\frac{\nu}{E}\sigma_x = -\nu\varepsilon_x, \quad \gamma_{x\theta} = \frac{\tau_{x\theta}}{G} \tag{22}$$

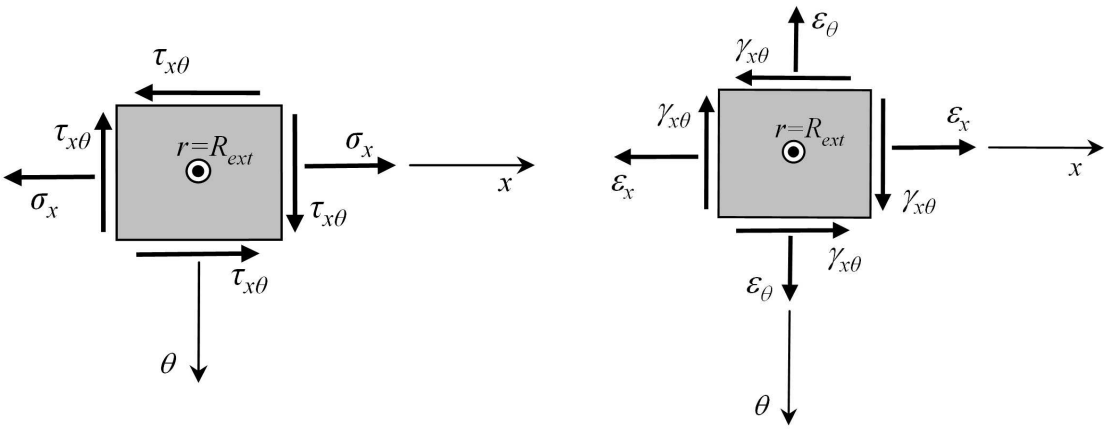

(a) Stress state. (b) Strain state.

Figure 6: Stress and strain states on the frame external surface (r=R_{ext}) in the cylindrical coordinate system.

Consider a linear strain gauge placed on the external surface at $x = x_i$, at a particular θ and with an angle β with respect to the beam axis (Figure 7); (x_1, x_2, x_3) is a local Cartesian coordinate system having x_2-axis along the strain gauge measurement axis, x_1-axis on the frame surface and x_3-axis normal to the frame surface and coincident with r-axis.

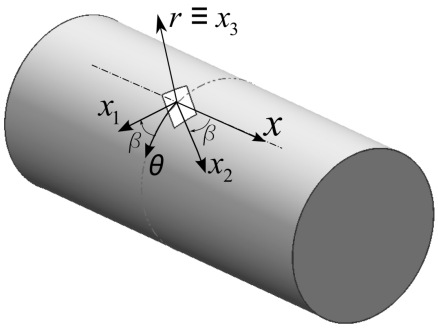

Figure 7: Location and coordinate system of a linear strain gauge placed on the frame external surface.

Using the appropriate strain-tensor transformations, from the (θ, x, r) to (x_1, x_2, x_3) coordinates [28], the relationship between the measured strain ε_2 and the strain tensor in Eq. (22) becomes

$$\varepsilon_2 = \varepsilon_x \cos^2\beta + \varepsilon_\theta \sin^2\beta + \gamma_{x\theta} \cos\beta \sin\beta \tag{23}$$

or, using the second of Eqs. (22),

$$\varepsilon_2 = \varepsilon_x \left(\cos^2\beta - \nu \sin^2\beta\right) + \gamma_{x\theta} \cos\beta \sin\beta \tag{24}$$

Expressing Eq. (2) for $r = R_{ext}$, yields [23-25]

$$\begin{aligned} \varepsilon_x &= e_1 + e_2 R_{ext} \sin\theta + e_3 R_{ext} \cos\theta \\ \gamma_{x\theta} &= e_4 \cos\theta - e_5 \sin\theta + e_6 R_{ext} \end{aligned} \tag{25}$$

Substituting Eq. (25) into Eq. (24) results in the relation between the measured strain ε_2 and the six strain measures at $x = x_i$

$$\begin{aligned} \varepsilon_2(x_i, \theta, \beta) = {} & e_1(x_i)\left(c_\beta^2 - \nu s_\beta^2\right) \\ & + e_2(x_i)\left(c_\beta^2 - \nu s_\beta^2\right) s_\theta R_{ext} \\ & - e_3(x_i)\left(c_\beta^2 - \nu s_\beta^2\right) c_\theta R_{ext} \\ & + e_4(x_i) c_\beta s_\beta c_\theta \\ & - e_5(x_i) c_\beta s_\beta s_\theta \\ & + e_6(x_i) c_\beta s_\beta R_{ext} \end{aligned} \tag{26}$$

where the following notation has been used: $c_\theta \equiv \cos\theta$, $s_\theta \equiv \sin\theta$, $c_\beta \equiv \cos\beta$, $s_\beta \equiv \sin\beta$.

4.2 Strain gauge distributions

The 0^{th}-order element, having constant e_1, e_4, e_5, and e_6 and linear e_2 and e_3, requires eight strain measurements. This number may be reduced to six by invoking the moment-shear equilibrium equations, Eq. (5). Substituting Eq. (4) into Eq. (5) results in

$$D_y e_{2,x} = G_z e_4, \quad D_z e_{3,x} = G_y e_5 \tag{27}$$

The 1^{st}-order element has constant e_1 and e_6, linear e_4 and e_5, and parabolic e_2 and e_3, thus requiring twelve strain measurements. For this element, each of the equations in Eqs. (27) is linear in x, thus four constraint equations are obtained; the number of the strain-gauge measurements is thus reduced from twelve to eight. This procedure should be viewed as a convenient means of reducing the required number of strain gauges by solving for e_4 and e_5 analytically rather than measuring these quantities experimentally. Since the magnitudes of e_4 and e_5 are generally much smaller compared to the bending strain measures, this treatment should be quite adequate for both static and dynamic applications. In Section 5, the validity of this constraint strategy for dynamically loaded beams is examined quantitatively.

Since the strain gauges can be placed anywhere along the beam surface, the distributions summarized in Table 1 are considered in this study (also refer to Figures 8 and 9); additional strain-gauge locations have been examined in [24]. To refer to a specific combination of the element type and strain-gauge configuration, a compact notation, #-#E, is used; where the first position, #, refers to the element order (0 or 1), the second position, #, indicates the number of strain gauges per element (6 or 8), and the letter "E" indicates that Eqs. (27) have been used in the formulation. The strain gauges are placed at different positions $x = (L^e/3, L^e/2, 2L^e/3)$ along the element. The strain-gauge angular orientations (θ, β) are also allowed to be different; for example, $(\theta, \beta) = (-2\pi/3, \pi/4)$ indicates that the strain gauge is placed at the circumferential angle $\theta=-2\pi/3$ and is oriented with an angle $\beta=\pi/4$ with respect to the frame x-axis (Figure 7).

Element-strain gauge notation	Orientation (θ, β) of strain gauges at $x=L^e/3$	Orientation (θ, β) of strain gauges at $x=L^e/2$	Orientation (θ, β) of strain gauges at $x=2L^e/3$
0-6E	-	$(-2\pi/3,0)$, $(-2\pi/3,\pi/4)$, $(0,0)$, $(0,\pi/4)$, $(2\pi/3,0)$, $(2\pi/3,\pi/4)$	-
1-8E	$(-2\pi/3,\pi/4)$	$(-2\pi/3,0)$, $(-2\pi/3,\pi/4)$, $(0,0)$, $(0,\pi/4)$, $(2\pi/3,0)$, $(2\pi/3,\pi/4)$	$(2\pi/3,\pi/4)$

Table 1: Strain-gauge distributions x, (θ, β) corresponding to the 0^{th}- and 1^{st} –order elements.

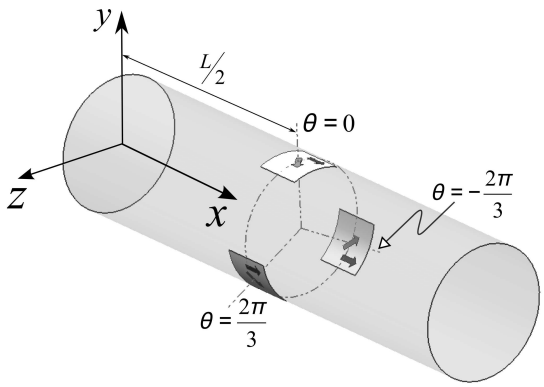

Figure 8: 0-6E strain gauge distribution.

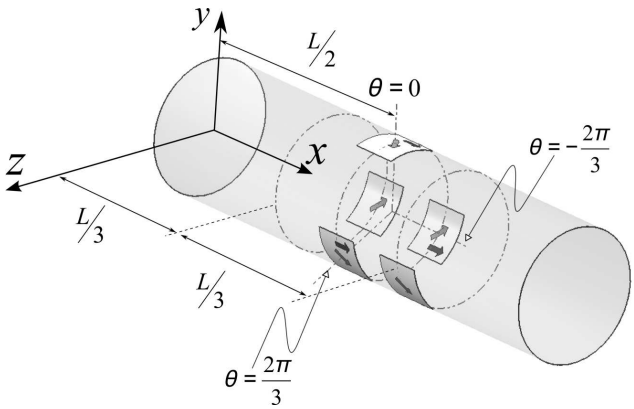

Figure 9: 1-8E strain gauge distribution.

5 NUMERICAL RESULTS

A simple cantilevered beam subjected to dynamic loading is analyzed to assess the accuracy of the inverse finite element method. The beam is made of an aluminum alloy (E=73,000 MPa, ν =0.3, and ρ=2557 Kg/m^3) and has a thin-walled circular cross-section with the average radius R =39 mm, wall thickness s=2 mm, and length L=800 mm. The beam is fully clamped on one end and subjected at the other end to a harmonic vertical force $F_z(t)$ (where t denotes time) acting in the z-direction at frequency f_0, i.e.,

$$F_z(t) = F_{z0} \sin\left(2\pi f_0 t\right) \tag{28}$$

where F_{z0} is the force amplitude (F_{z0} =10^3 N.) To simulate the experimental-strain measurements and to assess the accuracy of the inverse method, high-fidelity forward FE analyses are performed using QUAD4 shell elements in MSC/NASTRAN. The model consists of 114 elements along the cross-sectional circumference and 360 elements along the beam axis, for a total of 41,040 elements and 41,156 nodes. The tip force is applied at the cross-sectional center at a node which is connected to all other nodes within the cross-section by means of multi-point constraints (or MPC's) [29].

The dynamic response of the beam is calculated via a modal transient analysis keeping the modes up to 5,000 Hz, with the inclusion of viscous damping of magnitude 5% with respect to the critical value at each frequency. In the frequency range from 0 to 5,000 Hz, 51 modes are present: these include the first lowest flexural beam modes, 1F-5F, appearing twice due to the

cross-section symmetry, and the first membrane mode (1M). Table 2 summarizes the order of the global modes, their type, and corresponding frequency value f; the first three flexural mode shapes are shown in Figures 10-12. The other modes in the same frequency range are associated with the shell modes describing the cross-sectional distortion.

Mode order	1st and 2nd modes	3rd and 4th modes	12th mode	13th and 14th modes	30th and 31st modes	40th and 41st modes
Mode type	1F	2F	1M	3F	4F	5F
f frequency [Hz]	126.8	729.5	1,670	1,835	3,187	4,671

Table 2: Global modes of the cantilevered beam in the frequency range of 0-5,000 Hz. (F-type modes are flexural; M-type modes are membrane.)

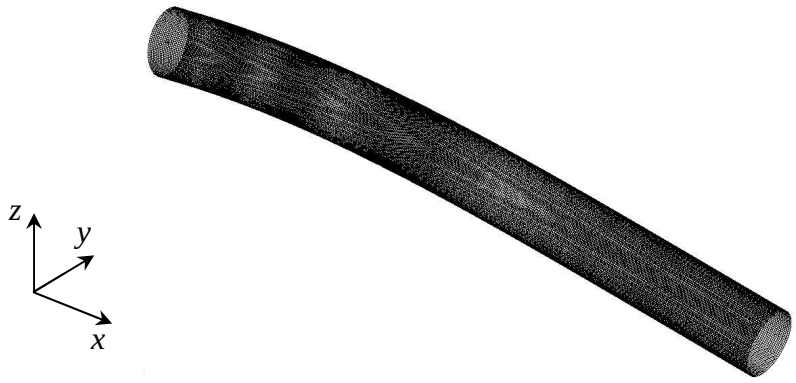

Figure 10: 1st flexural mode (1F, f = 126.8 Hz).

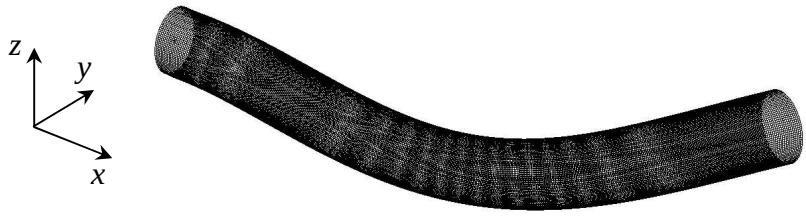

Figure 11: 2nd flexural mode (2F, f =729.5 Hz).

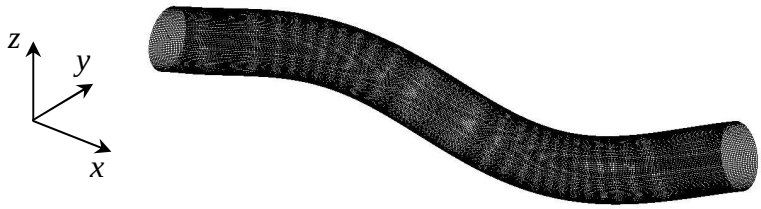

Figure 12: 3rd flexural mode (3F, f =1,835 Hz).

To investigate the accuracy of the iFEM modeling for dynamic applications in both low- and high-frequency regimes, three different values of the applied-force frequency f_0 have been con-

sidered, namely: f_0=60 Hz (about half of the fundamental frequency), f_0=450 Hz (halfway between 1F and 2F modes), and f_0=1,400 Hz (halfway between 2F and 3F). Figures 13-15 compare the tip-deflection time histories, $w_{max}(t)$, calculated by means of a high-fidelity FEM shell model using MSC/NASTRAN and the corresponding iFEM frame-element models. The tip deflection of the NASTRAN model corresponds to the cross-sectional center, and is computed at a node which is connected to all other nodes within the cross-section by means of MPC's. The present iFEM models used the strain-gauge distributions in Table 1 and the uniform weight coefficients $\lambda_k^0 = 1 \quad (k = 1,...,6)$ in Eq. (9); the strain values were taken from the nodes (at the specific locations in Table 1) of the NASTRAN model. It is noted that slightly more accurate strain values reside at the element Gauss points. However, considering the high fidelity of the reference FEM model, the "measured" strains taken at the nodes are quite satisfactory.

For the low-frequency loading of f_0=60 Hz, a single 0^{th}-order inverse element gives accurate results, with a maximum error in the tip deflection of 2.3% (Figure 13). At this excitation frequency, when $t \geq 0.1$, viscous damping has reduced the structural vibrations to a steady state response, proceeding at a constant amplitude and the same frequency as the forcing function. When the excitation frequency of the forcing function is increased, the response has a longer transient region, which is manifested by interactions between the natural modes of vibration and those due to the applied dynamic loading. To model the transient response at higher frequencies, finer discretizations are required. Thus, for f_0 = 450 Hz, a two-element, 1^{st}-order model yields a 1.1% error in the maximum deflection (Figure 14). At the f_0=1,400 Hz frequency, a three-element iFEM discretization using the 1^{st}- order element results in the maximum deflection error of 1.3% (Figure 15). These results clearly demonstrate that the methodology is highly efficient, requiring only few inverse elements and strain-gauge measurements, and is applicable not only for the steady state portion of the response but also for the transient regime at high frequencies.

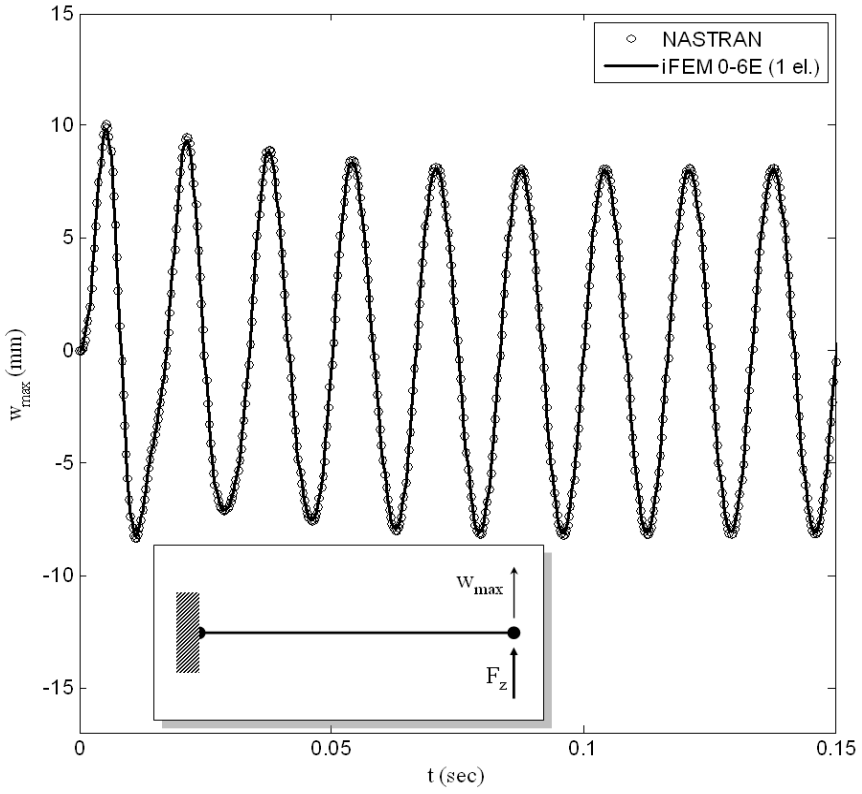

Figure 13: Tip deflection w_{max} of the beam loaded by a transverse concentrated force F_z at f_0=60 Hz.

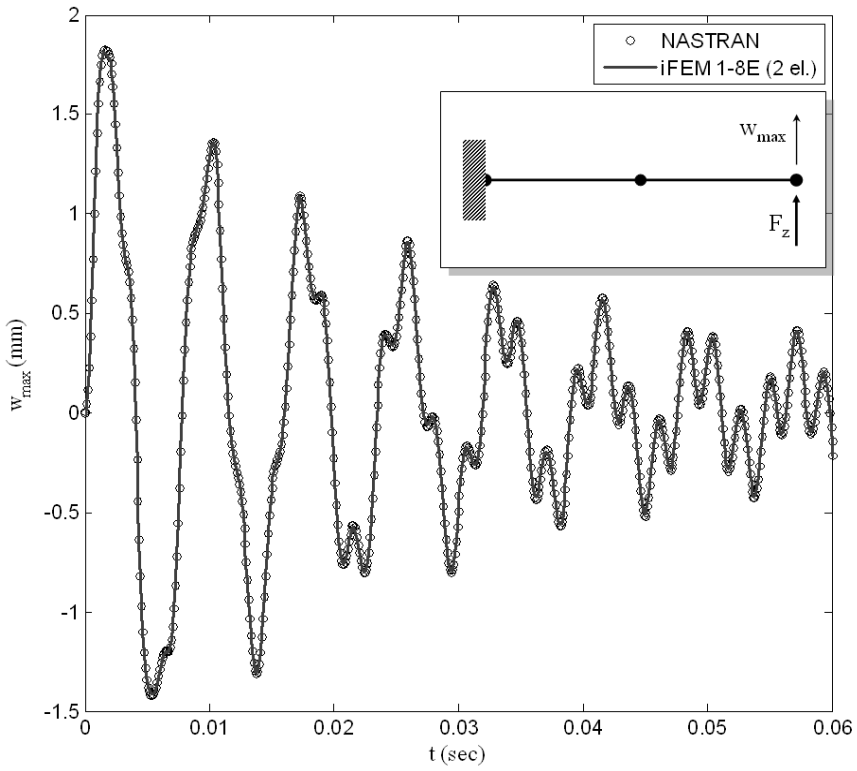

Figure 14: Tip deflection w_{max} of the beam loaded by a transverse concentrated force F_z at f_0=450 Hz.

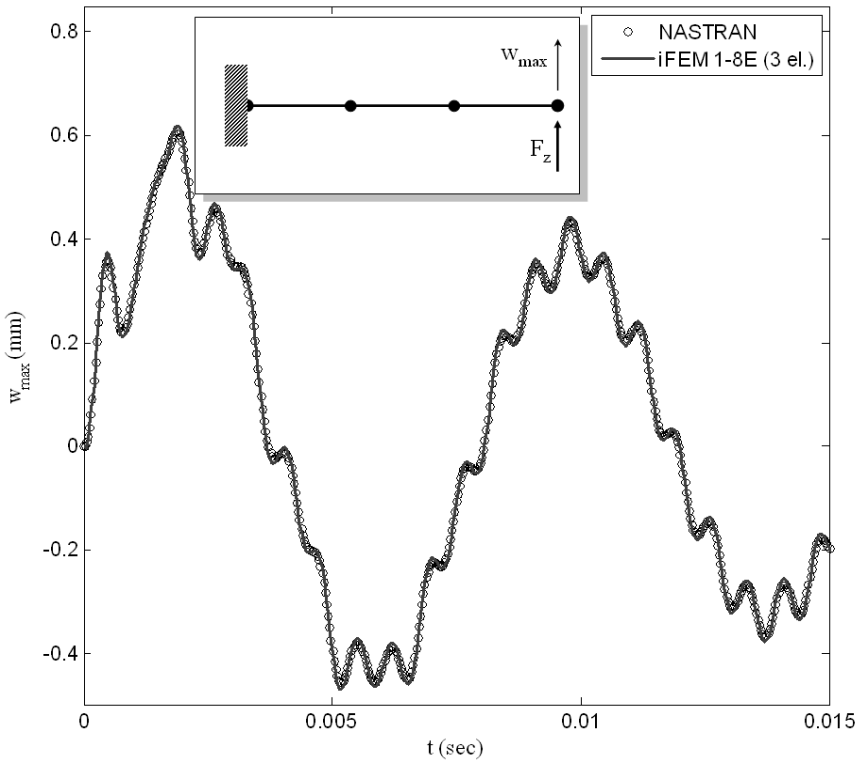

Figure 15: Tip deflection w_{max} of the beam loaded by a transverse concentrated force F_z at f_0=1,400 Hz.

6 CONCLUSIONS

In search of a suitable computational method for use in Structural Health Monitoring (SHM) systems, an inverse Finite Element Method (iFEM) has been formulated to perform the displacement-field reconstruction analysis (shape-sensing) of three-dimensional frame structures undergoing dynamic motion. The methodology uses a least-squares variational principle, which is discretized by C^0-continuous displacement-based *inverse* frame elements. Linear strain-displacement relations and their components, known as strain measures, are based on the Timoshenko (first-order) shear deformation theory that includes the deformations due to stretching, torsion, bending, and transverse shear. The variational statement enforces experimentally measured strains to be least-square compatible with those interpolated within the inverse frame elements. The implementation of this least-square compatibility is accomplished using the individual strain measures.

Two inverse frame elements, each having two nodes and twelve dof's, have been developed. The 0th-order element has a shear-strain measure which is constant along the element length; whereas the 1st-order element has a linear shear-strain measure. The element shape functions are based on interdependent interpolations that ensure free-of-shear-locking bending of slender frame members. The element interpolation order is linked to the definition of the number and orientation of the uniaxial strain gauges that are necessary for the analysis. Two simple and effective strain-gauge distributions have been selected and used in the numerical examples.

The present shape-sensing capability has been demonstrated on a thin-walled, circular cross-section cantilevered beam subjected to harmonic excitations in the presence of structural damping. To provide the *simulated* strain-gauge measurements, as well as the reference displacements, a high-fidelity shell finite element model was developed using the MSC/NASTRAN commercial code. Low- and high-frequency dynamic beam motions were analyzed and time history of the tip deflection examined, comparing several iFEM discretizations and strain-gauge schemes. The iFEM shape-sensing analysis, which is based only on the strain-displacement relations and the measured strain data (without any reliance on the material, inertial, or damping properties of the structure), has been shown to be highly effective and efficient in predicting the dynamic structural response of a damped beam. Accurate predictions of both the steady-state and transient response required only few elements and strain-gauge measurements, where the higher-frequency excitations necessitated somewhat higher fidelity of the iFEM models.

Although beyond the scope of the present effort, additional studies need to be performed, including: (a) shape-sensing analysis of spatial frame structures using the strains measured in a laboratory, and (b) studies of the strain-gauge distributions that provide optimal (or nearly optimal) solutions.

ACKNOWLEDGEMENTS

The first author acknowledges the support of Politecnico di Torino within the *Young Researchers Program 2010.*

REFERENCES

[1] A. Tessler, J.L. Spangler, A least-squares variational method for full-field reconstruction of elastic deformations in shear-deformable plates and shells, *Computer Methods in Applied Mechanics and Engineering*, **94**, 327–339, 2005.

[2] D.S. Schnur, N. Zabaras, Finite element solution of two-dimensional inverse elastic problems using spatial smoothing, *International Journal for Numerical Methods in Engineering*, **30**, 57–75, 1990.

[3] A.M. Maniatty, N.J. Zabaras, K. Stelson, Finite element analysis of some inverse elasticity problems, *Journal of Engineering Mechanics*, **115**, 1303–1317, 1989.

[4] A.M. Maniatty, N.J. Zabaras, Investigation of regularization parameters and error estimating in inverse elasticity problems, *International Journal for Numerical Methods in Engineering*, **37**, 1039–1052, 1994.

[5] P.L. Liu, H.T. Lin, Direct identification of non-uniform beams using static strains, *International Journal of Solids and Structures*, **33**, 2775–2787, 1996.

[6] M.A. Davis, A.D. Kersey, J. Sirkis, E.J. Friebele, Shape and vibration mode sensing using a fiber optic Bragg grating array, *Smart Materials and Structures*, **5**, 759–765, 1996.

[7] L.H. Kang, D.K. Kim, J.H. Han, Estimation of dynamic structural displacements using fiber Bragg grating strain sensors, *Journal of Sound and Vibration*, **305**, 534–542, 2007.

[8] N.S. Kim, N.S. Cho, Estimating deflection of a simple beam model using fiber optic Bragg-grating sensors, *Experimental Mechanics*, **44**, 433–439, 2004.

[9] W.L. Ko, W.L. Richards, V.T. Fleischer, Applications of the Ko displacement theory to the deformed shape predictions of the doubly-tapered Ikhana wing, *NASA/TP-2009-214652*, October 2009.

[10] P.B. Bogert, E.D. Haugse, R.E. Gehrki, Structural shape identification from experimental strains using a modal transformation technique, *44th AIAA/ASME/ASCE/AHS Structures, Structural Dynamics and Materials Conference*, Norfolk, Virginia, 2003.

[11] R.T. Jones, D.G. Bellemore, T.A. Berkoff, J.S. Sirkis, M.A. Davis, M.A. Putnam, E.J. Friebele, A.D. Kersey, Determination of cantilever plate shapes using wavelength division multiplexed fiber Bragg grating sensors and a least-squares strain-fitting algorithm, *Smart Materials and Structures*, **7**, 178–188, 1998.

[12] S. Shkarayev, R. Krashantisa, A. Tessler, An inverse interpolation method utilizing in-flight strain measurements for determining loads and structural response of aerospace vehicles, *3rd International Workshop on Structural Health Monitoring*, Stanford, California, 2001.

[13] S. Shkarayev, A. Raman, A. Tessler, Computational and experimental validation enabling a viable in-flight structural health monitoring technology, *1st European Workshop on Structural Health Monitoring*, Cachan, Paris, France, 2002.

[14] P. Mainçon, Inverse FEM I: Load and response estimates from measurements, *2nd International Conference on Structural Engineering, Mechanics and Computation*, Cape Town, South Africa, 2004.

[15] P. Mainçon, Inverse FEM II: Dynamic and non-linear problems, *2nd International Conference on Structural Engineering, Mechanics and Computation*, Cape Town, South Africa, 2004.

[16] A.J. Maree, P. Mainçon, Inverse FEM III: Influence of measurement data availability, *2nd International Conference on Structural Engineering, Mechanics and Computation*, Cape Town, South Africa, 2004.

[17] Barnardo, P. Mainçon, Inverse FEM IV: Influence of modelling error, *2nd International Conference on Structural Engineering, Mechanics and Computation*, Cape Town, South Africa, 2004.

[18] M. Nishio, T. Mizutani, N. Takeda, Structural shape reconstruction with consideration of the reliability of distributed strain data from a Brillouin-scattering-based optical fiber sensor, *Smart Materials and Structures*, **19**, 1-14, 2010.

[19] A. Tessler, J.L. Spangler, A variational principal for reconstruction of elastic deformation of shear deformable plates and shells, *NASA TM-2003-212445*, August 2003.

[20] A. Tessler, J.L. Spangler, Inverse FEM for full-field reconstruction of elastic deformations in shear deformable plates and shells, *2nd European Workshop on Structural Health Monitoring*, Munich, Germany, 2004.

[21] S.L. Vazquez, A. Tessler, C.C. Quach, E.G. Cooper, J. Parks, J.L. Spangler, Structural health monitoring using high-density fiber optic strain sensor and inverse finite element methods, *NASA TM-2005-213761*, May 2005.

[22] C.C. Quach, S.L. Vazquez, A. Tessler, J.P. Moore, E.G. Cooper, J.L. Spangler, Structural anomaly detection using fiber optic sensors and inverse finite element method, *AIAA Guidance, Navigation, and Control Conference and Exhibit*, San Francisco, California, 2005.

[23] M. Gherlone, Beam inverse finite element formulation, *LAQ Report Politecnico di Torino 1*, October 2008.

[24] P. Cerracchio, M. Gherlone, M. Mattone, M. Di Sciuva, A. Tessler, Inverse finite element method for three-dimensional frame structures, *DIASP Report Politecnico di Torino 285*, January 2010.

[25] P. Cerracchio, M. Gherlone, M. Mattone, M. Di Sciuva, A. Tessler, Shape sensing of three-dimensional frame structures using the inverse finite element method, *5th European Workshop on Structural Health Monitoring, Sorrento*, Italy, 2010.

[26] S.P. Timoshenko, On the correction for shear of differential equations for transverse vibrations of prismatic bars, *Philosophical Magazine*, **41**, 744–746, 1921.

[27] A. Tessler, S.B. Dong, On a hierarchy of conforming Timoshenko beam elements, *Computers & Structures*, **14**, 335–344, 1981.

[28] A.I. Lurie, *Theory of Elasticity*, Springer-Verlag Berlin Heidelberg, New York, 2005.

[29] MSC/MD-NASTRAN, *Reference Guide*, Version 2006.0, MSC Software Corporation, Santa Ana, CA.

[30] Bazoune, Y.A. Kulief, Shape functions of three-dimensional Timoshenko beam element, *Journal of Sound and Vibration*, **259-2**, 473–480, 2003.

APPENDIX

The 1st, 2nd, and 4th-degree Lagrange shape functions are given as

- 1st degree

$$\left[L_1^{(1)}, L_2^{(1)}\right] \equiv \frac{1}{2}\left[(1-\xi),(1+\xi)\right] \tag{A1}$$

- 2nd degree

$$\left[L_1^{(2)}, L_r^{(2)}, L_2^{(2)}\right] \equiv \frac{1}{2}\left[\xi(\xi-1), 2\left(1-\xi^2\right), \xi(\xi+1)\right] \tag{A2}$$

- 4th degree

$$\begin{aligned} \left[L_1^{(4)}, L_2^{(4)}\right] &\equiv \frac{1}{6}\xi\left(4\xi^2-1\right)\left[(\xi-1),(\xi+1)\right] \\ \left[L_q^{(4)}, L_r^{(4)}, L_s^{(4)}\right] &\equiv \frac{1}{3}\left(1-\xi^2\right)\left[4\xi(2\xi-1), 3\left(1-4\xi^2\right), 4\xi(2\xi+1)\right] \end{aligned} \tag{A3}$$

where $\xi \equiv 2x / L^e - 1 \in [-1,1]$ is a non-dimensional axial coordinate; $x \in \left[0, L^e\right]$ and L^e denotes the element length. The subscripts 1 and 2 represent the end nodes, whereas *q*, *r*, and *s* denote the uniformly spaced interior nodes.

The 3rd –degree shape functions, $N_j^{(3)}(\xi)$, of the 0th-order element have the form

$$\left[N_1^{(3)}, N_r^{(3)}, N_2^{(3)}\right] \equiv \frac{L^e}{24}\left(1-\xi^2\right)\left[(2\xi-3), -4\xi, (2\xi+3)\right] \tag{A4}$$

whereas the $\overline{N}_k^{(3)}(\xi)$ shape functions of the 1st-order element are

$$\left[\overline{N}_1^{(3)}, \overline{N}_q^{(3)}, \overline{N}_r^{(3)}, \overline{N}_s^{(3)}, \overline{N}_2^{(3)}\right] \equiv \frac{4}{3L^e}\left(1-\xi^2\right)\left[(4\xi-3), -2(8\xi-3), 24\xi, -2(8\xi+3), (4\xi+3)\right] \tag{A5}$$